Detailed study of the Milky Way globular cluster Laevens 3

Nicolas Longeard, Nicolas F. Martin, Rodrigo Ibata, Michelle Collins, Benjamin Laevens, Eric Bell, Dougal Mackey

Monthly Notices
of the
ROYAL ASTRONOMICAL SOCIETY

MNRAS **490,** 1498–1508 (2019)
Advance Access publication 2019 September 16

doi:10.1093/mnras/stz2592

Detailed study of the Milky Way globular cluster Laevens 3

Nicolas Longeard,[1]★ Nicolas Martin,[1,2] Rodrigo A. Ibata,[1] Michelle L. M. Collins,[3] Benjamin P. M. Laevens,[4] Eric Bell[5] and Dougal Mackey[6]

[1]*CNRS, Observatoire astronomique de Strasbourg, Université de Strasbourg, UMR 7550, F-67000 Strasbourg, France*
[2]*Max-Planck-Institut für Astronomy, Königstuhl 17, D-69117 Heidelberg, Germany*
[3]*Department of Physics, University of Surrey, Guildford, GU2 7XH Surrey, UK*
[4]*Institute of Astrophysics, Pontificia Universidad Católica de Chile, Av. Vicuña Mackenna 4860, 7820436 Macul, Santiago, Chile*
[5]*Department of Astronomy, University of Michigan, 500 Church St., Ann Arbor, 48109 MI, USA*
[6]*Research School of Astronomy and Astrophysics, Australian National University, Canberra, 2611 ACT, Australia*

Accepted 2019 September 10. Received 2019 September 9; in original form 2019 April 5

ABSTRACT

We present a photometric and spectroscopic study of the Milky Way satellite Laevens 3. Using MegaCam/Canada–France–Hawaii Telescope g and i photometry and Keck II/DEIMOS multi-object spectroscopy, we refine the structural and stellar properties of the system. The Laevens 3 colour–magnitude diagram shows that it is quite metal-poor, old (13.0 ± 1.0 Gyr), and at a distance of 61.4 ± 1.0 kpc, partly based on two RR Lyrae stars. The system is faint ($M_V = -2.8^{+0.2}_{-0.3}$ mag) and compact ($r_h = 11.4 \pm 1.0$ pc). From the spectroscopy, we constrain the systemic metallicity ($[\mathrm{Fe/H}]_{\mathrm{spectro}} = -1.8 \pm 0.1$ dex) but the metallicity and velocity dispersions are both unresolved. Using Gaia DR2, we infer a mean proper motion of $(\mu^*_\alpha, \mu_\delta) = (0.51 \pm 0.28, -0.83 \pm 0.27)$ mas yr^{-1}, which, combined with the system's radial velocity ($\langle v_r \rangle = -70.2 \pm 0.5$ km s^{-1}), translates into a halo orbit with a pericenter and apocenter of $40.7^{+5.6}_{-14.7}$ and $85.6^{+17.2}_{-5.9}$ kpc, respectively. Overall, Laevens 3 shares the typical properties of the Milky Way's outer halo globular clusters. Furthermore, we find that this system shows signs of mass segregation that strengthens our conclusion that Laevens 3 is a globular cluster.

Key words: Local Group.

1 INTRODUCTION

In recent years, the faint regime of Milky Way (MW) satellites has been explored under the impulsion of large photometric surveys. Among those, we can cite the Sloan Digital Sky Survey (York et al. 2000), the Panoramic Survey Telescope and Rapid Response System 1 (Chambers et al. 2016), or the Dark Energy Survey (The Dark Energy Survey Collaboration 2005). These surveys led to numerous discoveries of faint satellites. Several old and metal-poor faint systems have been identified as globular clusters (GCs; Balbinot et al. 2013; Laevens et al. 2014; Kim & Jerjen 2015; Kim et al. 2016), although some of them require confirmation (Martin et al. 2016c). Because of their old stellar populations, they can be considered as the witnesses of the formation of their host galaxy (Strader et al. 2005) and bring insights on low-mass galaxy formation. Furthermore, the chemodynamics of those GCs can also trace some of the current properties of their host (Pota et al. 2013). GCs can also be useful to constrain stellar population models (Chantereau, Charbonnel & Meynet 2016). The fact that these diffuse and small satellites survived for several billion years can also bring more information on their formation and internal processes (Baumgardt & Makino 2003; Renaud, Agertz & Gieles 2017).

The GCs associated with the MW span a wide range of luminosities, metallicities, and distances (Harris 2010), but only a few have been discovered in the outer reaches of the halo ($R_{\mathrm{gal}} > 50$ kpc). This specific group of clusters is in fact suspected to not have formed *in situ*, but rather as companions in nearby dwarf galaxies and accreted at later times in the MW history (Mackey et al. 2010; Dotter, Sarajedini & Anderson 2011). While clusters like Pal 14 (Arp & van den Bergh 1960, $d_{\mathrm{gal}} \sim 71$ kpc) or AM-1 (Madore & Arp 1979, $d_{\mathrm{gal}} \sim 125$ kpc) have been known for decades, only a handful of fainter outer halo clusters was discovered in recent photometric surveys. Laevens 1/Crater (Belokurov et al. 2014; Laevens et al. 2014) and Kim 2 (Kim et al. 2015) fall in this category. Such faint satellites often lie in the so-called 'valley of ambiguity' where the frontier between dwarf galaxies and old stellar clusters is not clearly defined (Gilmore et al. 2007). Laevens 1 is a great illustration of that, as its very nature was disputed at the time of its discovery. Indeed, while Laevens et al. (2014) identified the system as a cluster, Belokurov et al. (2014) proposed that the satellite could have been a tidally disrupted dwarf galaxy. This example only accentuates the hardship of studying these faint, distant stellar systems. In such an extreme regime, the combination of photometric, chemical, and kinematics data is needed to both classify and understand those systems.

★ E-mail: nicolas.longeard@astro.unistra.fr

Laevens 3 (Lae 3) is a system first discovered in the Pan-STARRS 1 (PS1; Chambers et al. 2016) data by Laevens et al. (2015). At the time, it was found to be compact ($r_h = 7 \pm 2$ pc) and the existence of an RR Lyrae star in this region, probably belonging to the system, allowed to constrain the distance to the system (64 ± 3 kpc). Using this distance, Laevens et al. (2015) found that the main sequence of Lae 3 was compatible with a stellar population of 8 Gyr, and a metallicity of [Fe/H] $= -1.9$. From these properties, the authors concluded that the system is a faint MW GC.

In this work, we undertake a careful refinement of the properties of the satellite through deep broad-band photometry with Canada–France–Hawaii Telescope (CFHT)/MegaCam, as well as the first spectroscopic follow-up of the system using Keck/DEIMOS (Faber et al. 2003). Section 2 discusses the technical aspects of our observations. Section 3 details the photometric analysis that derives the structural and colour–magnitude diagram (CMD) properties of the satellite. In Section 4, we present the dynamics of Lae 3 using multi-object spectroscopy, while Section 5 details the orbital properties of the satellite obtained with the Gaia Data Release 2 data. Finally, the nature and main properties of Lae 3 are discussed in Section 6.

2 OBSERVATIONS

2.1 Photometry

The photometry used in this work consists of multi-exposures MegaCam broad-band g- and i-band images. The exposure times are of 3×480 s for g and 3×540 s for i. The observations were conducted in service mode by the CFHT crew during the night of 2015 July 18, under excellent seeing conditions (~ 0.3 arcsec), and the data reduced following the procedure detailed in Longeard et al. (2018; L18). We use the Cambridge Astronomical Survey Unit (CASU; Irwin & Lewis 2001) pipeline flags to perform the star/galaxy separation. CASU also indicates all saturated sources. The calibration of the MegaCam photometry (Boulade et al. 2003) is performed on to the Pan-STARRS 1 (PS1) photometric system similar to L18. We first cross-identified all unsaturated point sources between PS1 and MegaCam. Only stars with photometric uncertainties below 0.05 in both catalogues are then considered for the calibration. We assume that the transformation between the PS1 and MegaCam photometry can be reliably modelled by a second-order polynomial, with a 3σ clipping procedure.

All stars saturated in the MegaCam photometry are directly imported from the PS1 catalog, for a total of 51 759 stars. Finally, the catalogue is dereddened using the 2D dust map from Schlegel, Finkbeiner & Davis (1998) to determine the line-of-sight extinction and Schlafly & Finkbeiner (2011) for the extinction coefficients.

2.2 Spectroscopy

The spectroscopic run for Lae 3 was performed on the night of 2015 September 7 (Julian date of 2457272.5) using Keck II/DEIMOS. The targets were selected based on their distance to Lae 3 and their location on the CMD, using the PS1 photometry presented in Laevens et al. (2015). A total of 51 stars were observed using the OG550 filter and the 1200 lines mm^{-1} grating. The typical central wavelength resolution is $R \sim 8500$, covering the spectral range from 6500 to 9000 Å. The spectra were then processed using the IRAF SIMULATOR package from the Keck Observatories and the pipeline detailed in Ibata et al. (2011). Stars with a signal-to-noise ratio below 3 as well as the ones with radial velocity uncertainties above 15 km s^{-1} are discarded from the spectroscopic catalogue. The resulting catalogue consists of 44 stars for which the spatial and CMD distributions are shown in Fig. 1. Finally, the instrumental systematic velocity uncertainty is chosen to be the same as in Longeard et al. (2019), with $\delta_{\rm thr} = 1.8^{+0.3}_{-0.2}$ km s^{-1}.

3 BROAD-BAND PHOTOMETRY ANALYSIS

The region including Lae 3 is shown in the left-hand panel of Fig. 1, with the stars observed spectroscopically colour-coded by their velocities. The central region of the system is densely populated. The CMD within two half-light radii of Lae 3 is shown in the right-hand panel of Fig. 1. The great depth of the MegaCam photometry allows us to probe the system two magnitudes below the main sequence turn-off and clearly reveals the main sequence of Lae 3. Our spectroscopic sample extends all the way down to the sub-giant branch, and suggests that Lae 3 possesses at least a few red giant branch (RGB) stars. Four RR Lyrae stars are located in the vicinity of the satellite according to the catalogue of Sesar et al. (2017). Among those, only stars with an RRab classification score greater than 90 per cent are selected, as the distance modulus measurement of RRc stars can be biased. Two stars pass this criterion and have a $m - M$ of 18.87 ± 0.06 and 18.89 ± 0.06 mag, respectively. By doing the mean of these two distance moduli, we obtain a distance modulus estimate of 18.88 ± 0.04 mag for Lae 3 ($59.7^{+0.2}_{-1.0}$ kpc in physical distance).

3.1 Structural and CMD fitting

We aim to derive the structural and stellar population properties of Lae 3. As such, we rely on the technique presented in Martin et al. (2016b) and L18. The stellar population parameters that we aim to infer are the age A, metallicity $[{\rm Fe/H}]_{\rm CMD}$, the α abundance ratio $[\alpha/Fe]$, and the distance modulus $m - M$. The structural properties that are determined are the spatial offsets of the centroid from the literature values ($\alpha = +316.72635^\circ$, $\delta = +14.98000^\circ$) X_0 and Y_0, the ellipticity ϵ,[1] the half-light radius r_h, the position angle of the major axis θ, and the number of stars $N*$ of the system within the data set.

To derive the structural parameters, the satellite is assumed to follow an exponential radial density profile, while the spatial density of the background is assumed to be constant over the field. The stellar characteristics are determined by assuming that the CMD of the satellite can be considered as the sum of two components: a unique stellar population for Lae 3, and a contamination from the foreground stars. Given the appearance of the Lae 3 sequence in Fig. 1, these assumptions are reasonable as the differences between isochrones in the metal-poor regime are not significant, except in the case of important spreads in both age and metallicity. The modelling of the CMD contamination is done empirically, by selecting all stars outside $5r_h$ of the system. The CMD of this sub-sample is further binned and smoothed by a Gaussian kernel of 0.1 in both colour and magnitude. The Lae 3 stellar population is, on the other hand, modelled using old and metal-poor isochrones from the Darmouth library (Dotter et al. 2008). The Lae 3 likelihood model is built by convolving each isochrone track by the typical photometric

[1]The ellipticity is defined as $\epsilon = 1 - \frac{a}{b}$, with a and b the major and minor axes of the ellipse, respectively.

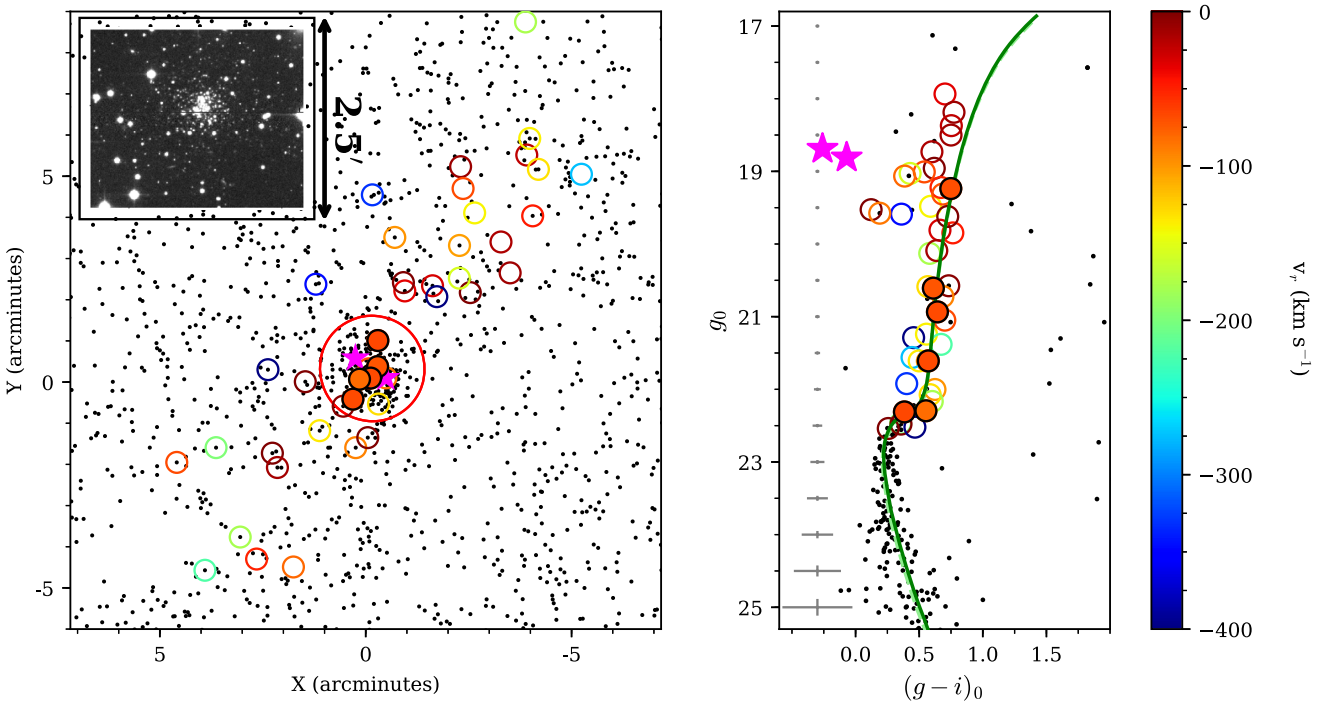

Figure 1. *Left-hand panel:* Spatial distribution of the Lae 3-like stellar population in the field of view. The CFHT image of the 2.5 arcmin × 2.5 arcmin region around Lae 3 in the i band is shown in the upper left-hand corner. The red circle represents the two half-light radii ($r_h \sim 0.64$ arcmin) region of Lae 3. The two RR Lyrae identified in the system are shown as the magenta stars. The spectroscopic data set is represented by the circles, colour-coded according to their heliocentric velocities. The filled circles stand for stars identified as Lae 3 members. *Right-hand panel:* CMD within two half-light radii of Lae 3. The best-fitting isochrone derived in Section 3.1 is represented as a solid green line, while the stellar population inferred without any distance or metallicity priors is represented by the light green dashed line. Photometric uncertainties are reported as the grey error bars on the left-hand side of the plot.

uncertainties of the data at a given (g_0, i_0). This model is then weighted by both the luminosity function of the track considered, and the completeness of the data at a given (g_0, i_0). This method is discussed in further details in L18.

The distance inferred using the RR Lyrae in the field can be used as a prior for our analysis. Moreover, and anticipating on Section 4, the spectroscopic analysis of three bright Lae 3 member stars allows us to infer the metallicity of the satellite to be $< [\mathrm{Fe/H}]_{\mathrm{spectro}} >= -1.8 \pm 0.1$ dex. The Probability Distribution Function (PDF) of this result can also be used as a prior.

The structural and CMD parameters are inferred all together and the results are displayed in Table 1, while the PDFs are shown in Fig. 2. We find that Lae 3 is spherical, with a half-light radius of 0.64 ± 0.05 arcmin that translates into a physical r_h of 11.4 ± 1.0 pc. The measured half-light radius is larger than that of the discovery paper (Laevens et al. 2015; ~ 0.4 arcmin). To investigate this discrepancy, the sample is split between bright ($15.0 < g_0 < 23.5$) and faint ($24.0 < g_0 < 25.0$) stars, and the structural properties of Lae 3 are derived in both cases. A significant difference arises in terms of half-light radius as shown in Fig. 3: the sample of bright stars yields a more compact size than with the faint end of the population. Such a discrepancy would naturally arise in a satellite in which a mass-segregation process has already occurred, and could explain the difference between this work and Laevens et al. (2015), who analysed the system with the shallower PS1 data. To test this, the structural analysis is performed using directly the PS1 data. The resulting PDF is shown as the dashed line in Fig. 3. The half-light radius inferred with this procedure is similar to the one obtained by L15, suggesting that the larger size derived from the MegaCam data is driven by less massive stars below $g < 22.5$ mag and that Lae 3 is mass segregated. We compute the relaxation time of Lae 3 using the equations of Koposov et al. (2007) and references therein to confirm that the satellite had enough time to mass segregate. We choose a mass-to-light ratio of 2 expected from old GCs (Bell & de Jong 2001), a total luminosity of 1125 $L_\odot$ determined below, and an average star mass of 0.6 $M_\odot$. The resulting half-light relaxation time is around 2.2 Gyr, largely smaller than our inference of the age of the satellite (13.0 ± 1.0 Gyr).

Two favoured stellar populations are presented in Fig. 2: with and without using the priors on the metallicity and distance modulus coming, respectively, from the spectroscopic analysis of Section 4 and the two RR Lyrae in the system. Without those priors, Lae 3 is found to be old (13.0 ± 1.0 Gyr) and metal-poor ($< [\mathrm{Fe/H}]_{\mathrm{CMD}} >= -2.0 \pm 0.1$ dex). The abundance ratio in α elements is $[\alpha/\mathrm{Fe}] = 0.2 \pm 0.2$ dex, while the distance modulus is $m - M = 19.05^{+0.02}_{-0.10}$ mag, i.e. a physical distance of $64.4^{+0.6}_{-3.0}$ kpc. This model is represented as a dashed light green line in Fig. 1 and nicely follows the sequence of the satellite and the spectroscopic members identified in the next section. The favoured model, i.e. the one based on the metallicity and distance priors, is similar. The structural properties, age, metallicity, and α abundance ratio are compatible. However, the satellite is found to be closer ($m - M = 18.94^{+0.05}_{-0.02}$ mag, which translates in a physical distance of $61.4^{+1.2}_{-1.0}$ kpc) in this case. This population, represented as a solid green line in Fig. 1, also follows the features of Lae 3 in the CMD. The two isochrones are barely distinguishable and the last model is the one used in the rest of this work since it is based on a spectroscopic measurement of the metallicity of the system. Using the favoured model, two quantities are defined: a 'CMD probability membership' that assigns a probability to a given star solely based

Table 1. Inferred properties of Lae 3.

Parameter	Unit	Prior	Favoured model	Uncertainties
RA α	deg	–	316.72938021	$\pm$0.00076375
			21:06:55:05	
DEC δ	deg	–	+14.98439985	$\pm$0.00077118
			+ 14:59:03:84	
l	deg	–	63.598	$\pm$0.001
b	deg	–	$-$21.176	$\pm$0.001
r_h	arcmin	> 0	0.64	$\pm$0.05
r_h	pc	> 0	11.4	$\pm$1.0
θ	deg	[0,180]	72	$^{+24}_{-17}$
ϵ	–	> 0	0.11	$^{+0.09}_{-0.11}$
Distance modulus	mag	$G(18.88, 0.04)$	18.94	$^{+0.05}_{-0.02}$
Distance	kpc		61.4	$^{+1.2}_{-1.0}$
Age	Gyr	[8.0,13.5]	13.0	$\pm$1.0
$[Fe/H]_{spectro}$	dex	–	$-$1.8	$\pm$0.1
$[\alpha/Fe]$	dex	[-0.2,0.6]	0.0	$\pm$0.2
M_V	mag	–	$-$2.8	$^{+0.2}_{-0.3}$
μ_0	mag arcsec^{-2}	–	25.0	$\pm$0.3
$< v_r >$	km s^{-1}	–	$-$70.2	$\pm$0.5
μ^*_α	mas yr^{-1}	–	0.51	$\pm$0.28
μ_δ	mas yr^{-1}	–	$-$0.83	$\pm$0.27
Apocenter	kpc	–	85.6	$^{+17.2}_{-5.9}$
Pericenter	kpc	–	40.7	$^{+5.6}_{-14.7}$
e_{orbit}	–	> 0	0.60	$^{+0.04}_{-0.06}$
U	km s^{-1}	–	13.1	$^{+64.2}_{-56.4}$
V	km s^{-1}	–	$-$187.3	$^{+45.1}_{-28.4}$
W	km s^{-1}	–	$-$211.8	$^{+59.0}_{-46.0}$
L_z	km s^{-1} kpc	–	793	$^{+4010}_{-3442}$
E	km^2 s^{-2}	–	20819	$^{+14822}_{-9163}$

on its compatibility with the favoured stellar population of Lae 3 and a 'CMD and spatial probability membership' that also takes the spatial location of a given star into account.

Using this CMD membership probability, we search for potential tidal structures. To do so, the field of view is spatially binned with 0.2 arcmin bins. The CMD probability of all stars falling in a given bin are then added. This procedure therefore assigns higher values to bins that contain stars compatible with the stellar population of Lae 3. The result is shown in Fig. 4. This analysis shows that the satellite is highly spherical and that there is no tidal feature in the field of view compatible with the CMD properties of Lae 3.

The luminosity of the satellite is estimated following the method detailed in Martin et al. (2016a) that consists in simulating thousands of CMDs with the stellar and structural properties of Lae 3 derived earlier, and compute their resulting luminosities. This procedure yields a luminosity of $L_V = 1125^{+221}_{-129}\,L_\odot$, translating into an absolute magnitude of $M_V = -2.8^{+0.2}_{-0.3}$ mag. This result is roughly one magnitude fainter than that found by Laevens et al. (2015) in the discovery paper of Lae 3. We observed a similar trend for another faint satellite discovered by Laevens et al. (2015): Draco II (Dra II). In L18, the inferred luminosity was significantly lower than found in the 2015 paper, and we concluded that it is most likely due to the overestimation of the number of giants in the system, probably due to the shallowness of the PS1 data used for the discovery of both Lae 3 and Dra II. Though Lae 3 is clearly brighter than Dra II, it is also significantly more distant, and the same overestimation effect might have affected the result of Laevens et al. (2015), as using the same technique for a brighter MW satellite (Longeard et al. 2019) did not yield such an effect.

4 SPECTROSCOPIC ANALYSIS

The distribution of the heliocentric velocities for all stars in our spectroscopic sample is shown in the top panel of Fig. 5, along with their radial distances and spectroscopic metallicities (if possible). The properties of the entire sample are described in Table 2.

4.1 Dynamical properties

The Lae 3 population is not prominent, and its systemic velocity overlaps that of the foreground MW stars (Fig. 5). Our approach is similar to L18: the velocity distribution is assumed to be the sum of the contamination (halo and disc stars) and the Lae 3 population, both modelled with different normal distributions. To highlight Lae 3's population in the spectroscopic data set, the individual likelihood of each star is weighted by its spatial and CMD probability estimated from the favoured structural model of Section 3 (Collins et al. 2010). This analysis yields a systemic radial velocity of $< v_r >= -70.2 \pm 0.5$ km s^{-1}. The 1D marginalized PDFs of the velocity parameters are represented in the left-hand panels of Fig. 6. As a consequence to the low number of Lae 3 stars, the velocity dispersion is unresolved. Finally, six stars with a dynamical, structural, and CMD membership probability greater than 90 per cent are identified as Lae 3 members and shown as the filled circles in Fig. 5.

4.2 Spectroscopic metallicity

The individual metallicities of stars observed with spectroscopy can be estimated using the calibration of the Calcium triplet (Starken-

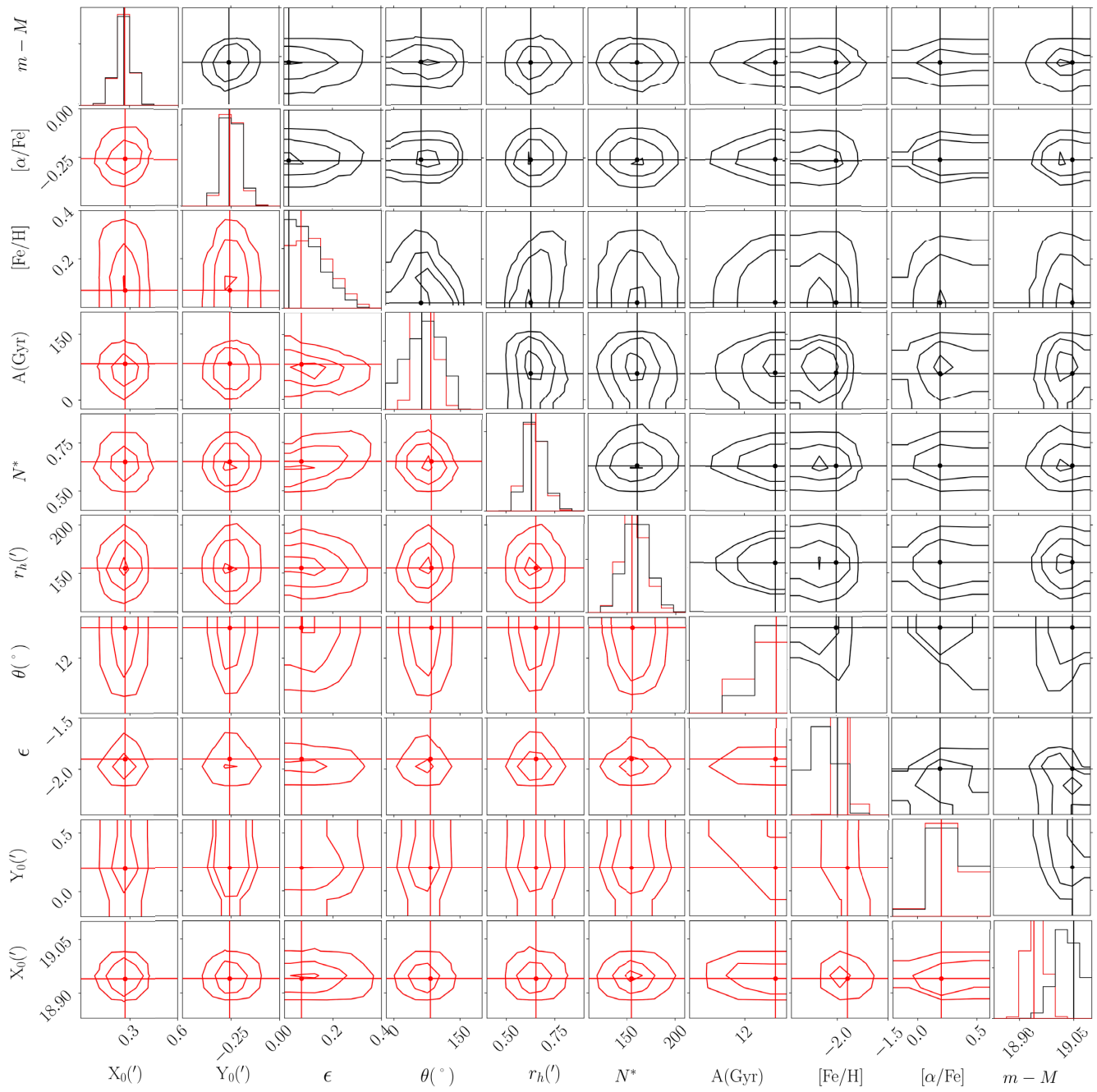

Figure 2. 1D and 2D posterior PDFs of the structural and CMD parameters of Lae 3, inferred using the method described in Section 3.1. Contours correspond to the usual 1σ, 2σ, and 3σ confidence intervals in the case of a 2D Gaussian. The red solid lines correspond to the analysis using both the distance and metallicity priors described in Section 3, while the black lines represent the case without any prior applied. The black and red dots correspond to the favoured model in each case.

burg et al. 2010) for RGB stars, and shown in Fig. 5. Member stars fainter than 21 in the g band, and with S/N < 10 are further discarded from our spectroscopic catalogue. Only three stars are left to infer the systemic metallicity and metallicity dispersion of Lae 3, by assuming that the metallicities are normally distributed. This yields a spectroscopic metallicity of $[\mathrm{Fe/H}]_{\mathrm{spectro}} = -1.8 \pm 0.1$ dex. The same analysis is also performed using the calibration of Carrera et al. (2013) for metal-poor stars on the RGB and sub-RGB branch, and yields compatible results. Once more, low-number statistics has a direct consequence on our ability to constrain efficiently the metallicity dispersion, which is found to be unresolved, with $\sigma_{[\mathrm{Fe/H}]} < 0.5$ dex at the 95 per cent confidence level. The PDFs of both parameters are shown in the right-hand panels of Fig. 6.

5 GAIA DR2 PROPER MOTIONS AND ORBIT

To infer the orbital properties of Lae 3, we cross-match all spectroscopic members and RR Lyrae stars with the Gaia Data Release 2 (Gaia Collaboration 2018). Among those, four stars have a proper motion (PM) measurement in Gaia. Furthermore,

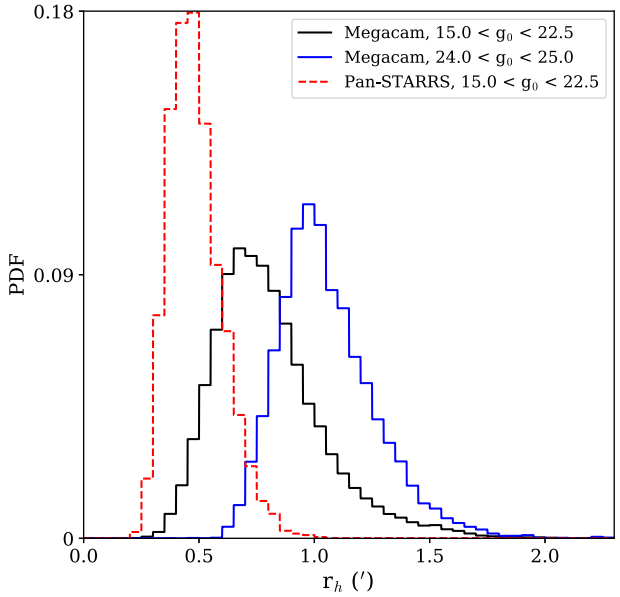

Figure 3. 1D PDFs of the half-light radius of Lae 3 in three cases: using stars with $15.0 < g_0 < 22.5$ in MegaCam (the solid black line), stars with $24.0 < g_0 < 25.0$ (the solid blue line) in MegaCam, and the PS1 catalog (the dashed red line). The magnitude ranges in the first two cases were chosen so that the inferred numbers of Lae 3 stars are similar. Lae 3 comes out as larger when considering lower mass stars than when the analysis is performed on a more massive sample, hinting at a mass-segregation process. The size of the satellite inferred by L15 is retrieved when using their data, indicating that this effect is not caused by a problem in our approach or a statistical fluke.

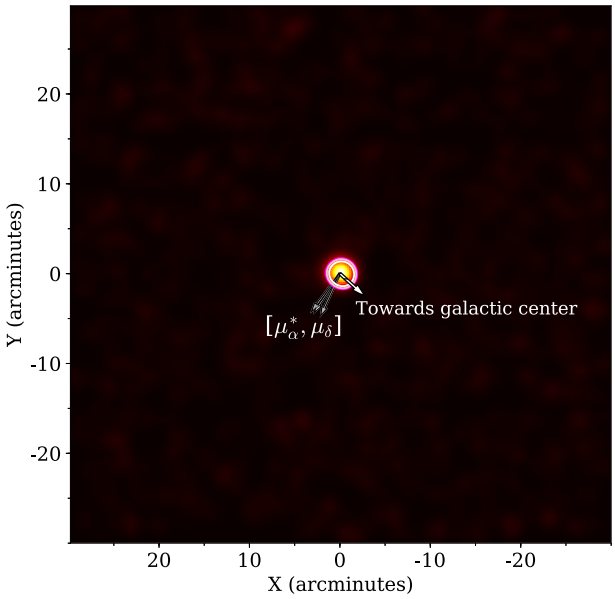

Figure 4. Density plot for all stars with $P_{mem} > 0.01$ over the field of view. The magenta, pink, and white lines outline the regions with a density higher than 68, 95, and 99 per cent of the background pixel distribution. The proper motion of Lae 3 is shown with the grey arrows along with its uncertainties, while the direction towards the Galactic centre is indicated with a white arrow. No tidal features is detected in the vicinity of the satellite.

all stars in the Gaia catalog with a CMD and structural membership probability greater than 90 per cent are included. Six additional stars are retrieved through this procedure, and their PMs are compatible with those of the spectroscopic members, as shown in Fig. 7. The uncertainty-weighted average PM of Lae 3 yields $\mu_\alpha^{*,\mathrm{Lae3}} = \mu_\alpha^{\mathrm{Lae3}} \cos(\delta) = 0.51 \pm 0.28$ mas yr^{-1} and $\mu_\delta^{\mathrm{Lae3}} = -0.83 \pm 0.27$ mas yr^{-1}. These measurements take into account the systematic error of 0.035 mas yr^{-1} on the PMs for dSph as shown by Helmi et al. (2018). We point out that this choice of systematic error does not change our results, given the measured uncertainties on the PM of the satellite.

We use the GALPY package (Bovy 2015) to integrate the orbit of Lae 3. The MW potential chosen to integrate Lae 3 orbit is a variant of the 'MWPotential14' defined within GALPY, but updated with a halo mass of 1.2×10^{12} M$_\odot$ (Bland-Hawthorn & Gerhard 2016). A total of 5000 orbits are integrated backwards and forwards over 5 Gyr, each time by randomly drawing a position, distance, radial velocity, and PMs from their corresponding PDFs. Around 20 per cent of the resulting orbits are not bound to the MW. In the case where Lae 3 is bound to the MW, the pericenter is at $40.7^{+5.6}_{-14.7}$ kpc and the apocenter is at $85.6^{+17.2}_{-5.9}$ kpc. The favoured orbit of the satellite is shown as a solid blue line in Fig. 8 and corresponds to a typical outer halo orbit. In the unbound case, the apocenter is undefined and the pericenter is larger, at $59.1^{+0.7}_{-2.1}$ kpc.

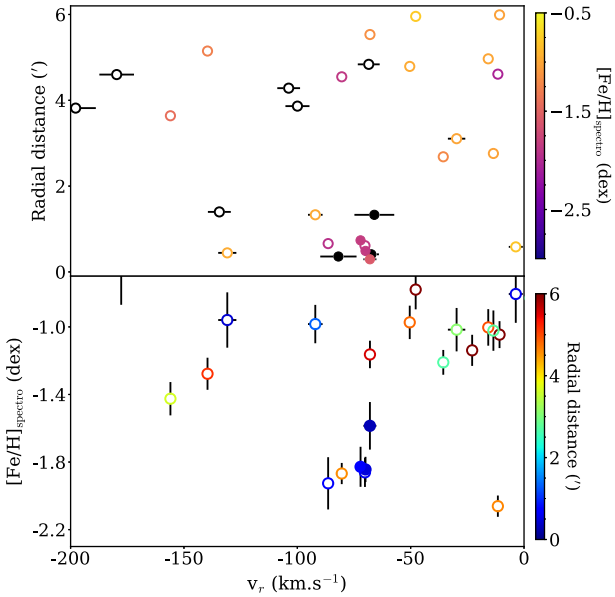

Figure 5. Heliocentric velocities versus radial distances (top panel) and spectroscopic metallicities (bottom panel). The coloured circles are non-HB stars with an S/N greater than 10, for which we are able to derive the spectroscopic metallicities. The colour maps stand for the metallicity (top) and radial distance (bottom). The spectroscopic members are shown as the filled dots.

6 DISCUSSION AND CONCLUSIONS

We present in this paper an analysis of the faint satellite Lae 3 using deep MegaCam/CFHT broad-band g- and i-band photometry of Lae 3 as well as multi-object spectroscopy observed with Keck II/DEIMOS. Lae 3 has a systemic velocity that overlaps with the MW foreground contamination: $\langle v_r \rangle = -70.2 \pm 0.5$ km s^{-1}, but an unresolved velocity dispersion. Using these results, six stars are unambiguously identified as Lae 3 members, and three are bright enough to be used to estimate the systemic metallicity of the satellite. Lae 3 comes out as a fairly metal-poor stellar

Table 2. Properties of our spectroscopic sample. Confirmed members are denoted by 'Y' and non-members by 'N'. The star denoted 'Y?' is a plausible member, as its position, spectroscopic metallicity, and velocity are compatible with those of Lae 3. However, it is not confirmed as it does not pass our membership probability cut ($P_{\rm mem} \geq 90$ per cent).

RA (deg)	Dec. (deg)	g_0	i_0	v_r (km s^{-1})	μ_α^* (mas yr^{-1})	μ_δ (mas yr^{-1})	S/N	(Fe/H)$_{\rm spectro}$	$P_{\rm mem}$	Member
316.71305417	15.01271111	17.94 ± 0.01	17.23 ± 0.01	−35.6 ± 1.4	3.647 ± 0.221	−3.548 ± 0.242	39.3	−1.21 ± 0.07	0.00	N
316.68967917	15.06302222	18.19 ± 0.01	17.41 ± 0.01	−10.8 ± 1.4	−0.763 ± 0.239	−0.821 ± 0.254	36.3	−1.05 ± 0.08	0.00	N
316.67275417	15.03253056	18.73 ± 0.01	18.13 ± 0.01	−15.8 ± 1.7	−5.232 ± 0.413	−8.422 ± 0.403	22.1	−1.0 ± 0.11	0.00	N
316.68561250	15.01203889	18.96 ± 0.01	18.34 ± 0.01	8.1 ± 2.1	−2.672 ± 0.44	−6.607 ± 0.465	21.9	−1.15 ± 0.1	0.00	N
316.68863750	15.05416944	19.01 ± 0.01	18.47 ± 0.01	−68.0 ± 1.4	−1.407 ± 0.459	−2.176 ± 0.464	26.9	−1.16 ± 0.08	0.00	N
316.69020000	15.01787500	19.03 ± 0.01	18.60 ± 0.01	−156.0 ± 1.6	−2.898 ± 0.505	−7.339 ± 0.511	20.0	−1.43 ± 0.1	0.00	N
316.68378750	15.04429167	19.48 ± 0.01	18.89 ± 0.01	−139.6 ± 1.6	−2.633 ± 0.625	−13.336 ± 0.613	23.3	−1.28 ± 0.09	0.00	N
316.71363750	15.01609167	19.53 ± 0.01	19.41 ± 0.01	429.0 ± 2.6	−0.284 ± 0.873	−0.101 ± 0.927	20.8	−2.95 ± 0.14	0.00	N
316.75032500	15.01542778	19.59 ± 0.01	19.23 ± 0.01	−346.7 ± 1.6	−2.236 ± 0.853	−1.489 ± 0.947	24.0	−1.96 ± 0.08	0.00	N
316.70143333	15.01480278	19.81 ± 0.01	19.15 ± 0.01	−29.7 ± 3.8	−4.405 ± 0.758	−0.392 ± 0.796	18.5	−1.02 ± 0.13	0.01	N
316.69964167	15.01039167	21.29 ± 0.01	20.83 ± 0.01	−515.3 ± 3.0	– ± –	– ± –	9.1	– ± –	0.00	N
316.69013750	15.03111667	21.61 ± 0.01	21.05 ± 0.01	−103.8 ± 5.0	– ± –	– ± –	8.0	– ± –	0.01	N
316.72665833	15.05161389	21.92 ± 0.01	21.52 ± 0.01	−331.2 ± 3.6	– ± –	– ± –	5.4	– ± –	0.00	N
316.71725417	15.03437222	22.00 ± 0.01	21.38 ± 0.01	−99.9 ± 5.3	– ± –	– ± –	6.4	– ± –	0.01	N
316.72435000	14.99263333	22.31 ± 0.02	21.93 ± 0.02	−66.0 ± 8.8	– ± –	– ± –	4.3	– ± –	0.99	Y
316.66194583	15.06772222	18.37 ± 0.01	17.62 ± 0.01	−229 ± 1.4	1033 ± 0.276	0.696 ± 0.289	30.0	−1.14 ± 0.09	0.00	N
316.66891250	15.02001944	18.50 ± 0.01	17.75 ± 0.01	−11.5 ± 1.1	1.047 ± 0.322	−1.302 ± 0.317	29.3	−2.06 ± 0.06	0.00	N
316.65947083	15.04309444	19.85 ± 0.01	19.08 ± 0.01	−47.8 ± 1.9	−3.144 ± 0.76	−4.985 ± 0.724	20.7	−0.78 ± 0.12	0.00	N
316.66246667	15.12159167	20.13 ± 0.01	19.55 ± 0.01	−177.7 ± 2.8	0.483 ± 1.105	−6.195 ± 0.963	21.7	−0.61 ± 0.26	0.00	N
316.66070833	15.07443611	21.24 ± 0.01	20.68 ± 0.01	−138.4 ± 4.7	– ± –	– ± –	9.5	– ± –	0.00	N
316.63902917	15.05994444	21.56 ± 0.01	21.12 ± 0.01	−274.5 ± 11.8	– ± –	– ± –	5.9	– ± –	0.00	N
316.65706250	15.06192222	22.07 ± 0.01	21.49 ± 0.01	−131.8 ± 6.9	– ± –	– ± –	5.0	– ± –	0.00	N
316.80862500	14.94329722	21.05 ± 0.01	20.35 ± 0.01	−68.5 ± 4.8	– ± –	– ± –	12.2	– ± –	0.00	N
316.79680833	14.89963056	21.38 ± 0.01	20.71 ± 0.01	−221.0 ± 4.5	– ± –	– ± –	8.7	– ± –	0.00	N
316.79215417	14.94927500	22.47 ± 0.02	22.11 ± 0.02	−197.8 ± 8.9	– ± –	– ± –	3.3	– ± –	0.13	N
316.75973333	14.90096111	19.07 ± 0.01	18.68 ± 0.01	−80.4 ± 2.0	0.335 ± 0.641	−2.754 ± 0.557	26.2	−1.87 ± 0.06	0.00	N
316.77516250	14.90417500	19.22 ± 0.01	18.55 ± 0.01	−50.4 ± 1.9	−1.68 ± 0.596	−8.502 ± 0.498	27.5	−0.97 ± 0.1	0.00	N
316.72701667	14.97872778	19.24 ± 0.01	18.49 ± 0.01	−69.9 ± 1.6	1.565 ± 0.53	−1.232 ± 0.523	23.3	−1.84 ± 0.07	0.98	Y
316.72812500	14.98119167	19.31 ± 0.01	18.63 ± 0.01	−70.2 ± 1.4	0.31 ± 0.608	−0.609 ± 0.592	22.5	−1.86 ± 0.09	0.36	Y?
316.72099583	14.97752500	19.58 ± 0.01	19.39 ± 0.01	−86.4 ± 2.1	0.758 ± 0.852	2.285 ± 0.871	20.0	−1.93 ± 0.15	0.00	N
316.76855417	14.94703889	19.62 ± 0.01	18.90 ± 0.01	2.9 ± 1.8	−4.84 ± 0.79	−3.869 ± 0.784	25.6	−0.83 ± 0.1	0.16	N
316.76643750	14.94122778	20.09 ± 0.01	19.45 ± 0.01	−13.5 ± 2.3	−2.702 ± 1.02	−5.581 ± 1.006	19.0	−1.02 ± 0.12	0.02	N
316.73886667	14.96605556	20.57 ± 0.01	19.84 ± 0.01	−3.6 ± 3.1	−1.88 ± 1.572	−1.143 ± 1.61	15.6	−0.81 ± 0.17	0.45	N
316.72408750	14.96693889	20.59 ± 0.01	20.02 ± 0.01	−130.9 ± 4.0	1.839 ± 2.395	−0.506 ± 1.892	14.5	−0.96 ± 0.16	0.63	N
316.72444583	14.98208333	20.61 ± 0.01	20.00 ± 0.01	−72.1 ± 1.7	−0.0 ± 2.13	0.456 ± 2.024	15.0	−1.83 ± 0.12	0.99	Y
316.73362500	14.94926389	20.72 ± 0.01	20.04 ± 0.01	−92.1 ± 3.2	−0.211 ± 2.05	−3.577 ± 2.068	14.5	−0.98 ± 0.11	0.86	N
316.73480000	14.96889167	20.93 ± 0.01	20.29 ± 0.01	−68.0 ± 2.9	– ± –	– ± –	13.3	−1.59 ± 0.14	1.00	Y
316.74872917	14.95614167	21.61 ± 0.01	21.11 ± 0.01	−134.4 ± 5.1	– ± –	– ± –	8.2	– ± –	0.09	N
316.72737500	14.97743611	21.61 ± 0.01	21.04 ± 0.01	−67.4 ± 3.4	– ± –	– ± –	7.5	– ± –	1.00	Y
316.78203333	14.91307778	22.17 ± 0.01	21.56 ± 0.01	−179.7 ± 7.6	– ± –	– ± –	5.3	– ± –	0.00	N
316.73203333	14.97697778	22.30 ± 0.02	21.74 ± 0.02	−81.9 ± 8.0	– ± –	– ± –	4.5	– ± –	1.00	Y
316.72857917	14.95332778	22.48 ± 0.02	22.12 ± 0.02	60.1 ± 9.2	– ± –	– ± –	3.5	– ± –	1.00	N
316.77040833	14.98083611	22.52 ± 0.02	22.05 ± 0.02	−437.6 ± 3.9	– ± –	– ± –	4.1	– ± –	0.07	N
316.75475417	14.97596389	22.54 ± 0.02	22.28 ± 0.02	738.4 ± 15.1	– ± –	– ± –	3.2	– ± –	1.00	N

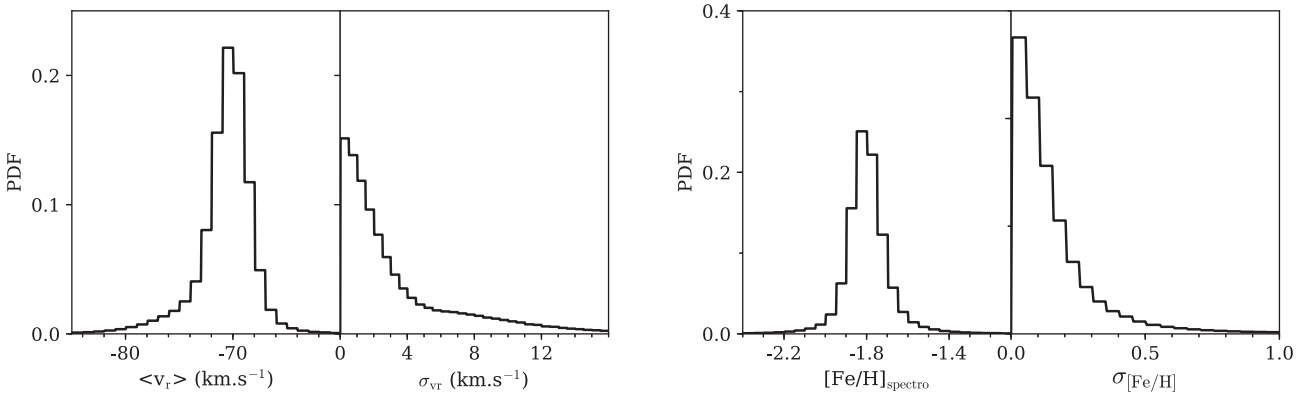

Figure 6. *Left-hand panels:* 1D marginalized PDFs of the systemic velocity and its associated dispersion. *Right-hand panels:* 1D marginalized PDFs of the systemic metallicity and its associated dispersion. The two measurements of the dispersions are unresolved.

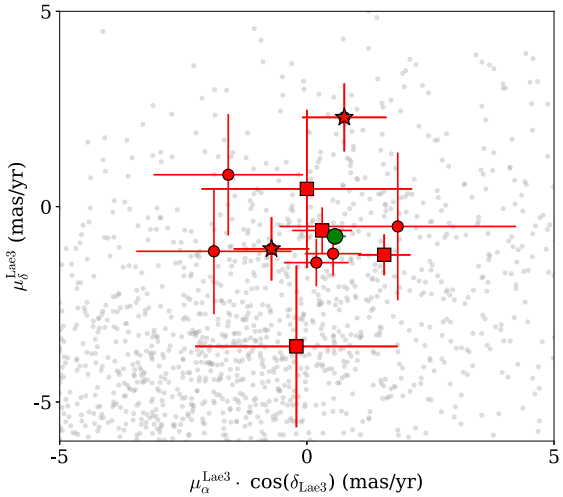

Figure 7. PMs of all stars within 15′ of Lae 3. The grey transparent dots show the PMs of field stars. The measurements of the four spectroscopic members with PM in Gaia DR2 are represented as the squares, while the red stars and the dots, respectively, show the PMs of the RR Lyrae stars as well as the spatially and CMD selected stars. The large green dot marks the combined PM measurement of Lae 3.

system: $\langle[\mathrm{Fe/H}]_{\mathrm{spectro}}\rangle = -1.8 \pm 0.1$ dex that places Lae 3 far off the luminosity–metallicity relation of dwarf galaxies (Kirby et al. 2013) as shown in Fig. 9. The metallicity dispersion is also unresolved. Similar to Laevens et al. (2015), two RR Lyrae stars are used to estimate the distance of Lae 3, and yield a distance modulus of 18.88 ± 0.04 mag. Using these results as priors, we derive the structural and CMD properties and find a half-light radius of 11.4 ± 1.0 pc, a marginally resolved ellipticity and a final distance modulus measurement of $18.94^{+0.05}_{-0.02}$ mag. A discrepancy between the half-light radius of Lae 3 derived using bright and faint stars hints that the satellite is mass segregated. This hypothesis is strengthened by the relaxation time of the satellite of ~ 2.2 Gyr, much smaller than the age of the satellite found to be 13.0 ± 1.0 Gyr by our CMD fitting procedure. The sphericity of Lae 3 and an analysis of the density of Lae 3-like stars in the field show no clear sign of tidal features that might hint at a perturbation of the system and therefore its ability to mass segregate. The favoured stellar population is metal-poor, not particularly enriched in α elements, and at a distance of $61.4^{+1.2}_{-1.0}$ kpc. Finally, the orbit calculation yields an outer halo orbit, with a pericenter of $40.7^{+5.6}_{-14.7}$ kpc and an apocenter of $85.6^{+17.2}_{-5.9}$ kpc.

Lae 3 shows the main characteristics of MW GCs: the satellite is fairly spherical and is at the same time more compact and metal-rich than DGs of the same luminosity (McConnachie 2012; Kirby et al. 2013), such as Ret II ($M_V \sim -2.7$), Hor I ($M_V \sim -3.4$)

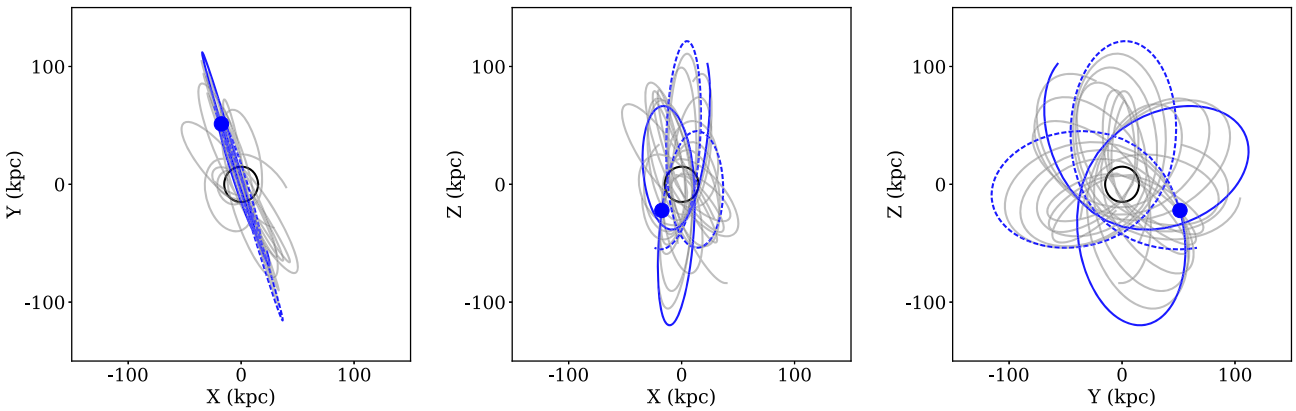

Figure 8. Orbits of Lae 3 in the *X*–*Y*, *X*–*Z*, and *Y*–*Z* planes integrated over 5 Gyr. The blue line is the orbit for the favoured distance, radial velocity, position, and proper motion. The grey, transparent lines are random realizations of the orbit. The MW is represented by the black circle ($R_{\mathrm{MW}} = 15$ kpc), while the blue dot indicates the location of Lae 3 at present day.

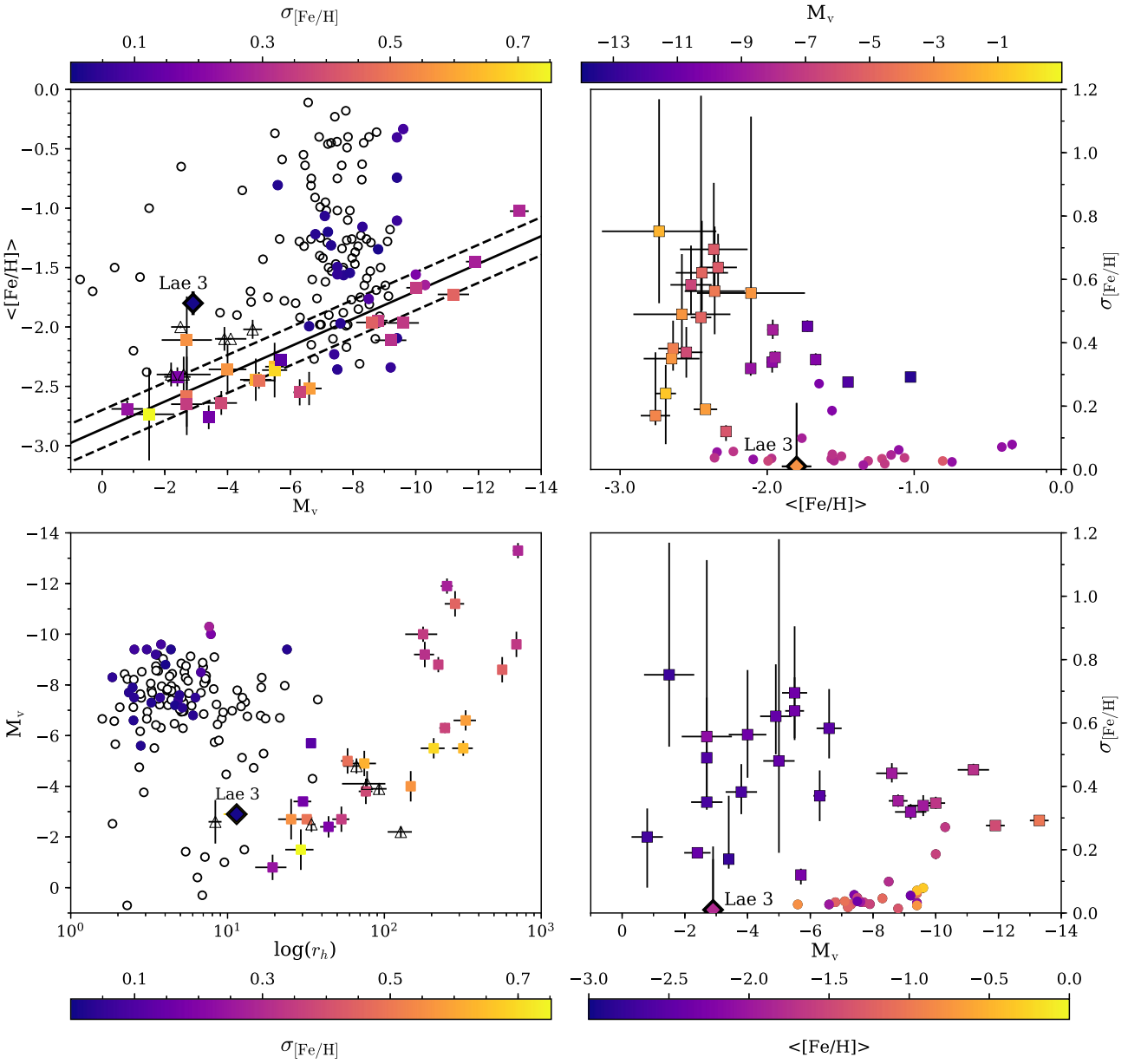

Figure 9. Comparison of Lae 3 with other GCs and dwarf galaxies of the Milky Way. The squares represent dwarf galaxies, while the circles represent globular clusters, and the diamond corresponds to Lae 3. The triangles stand for recently discovered dwarf-galaxy candidates that await confirmation. The hollow markers correspond to systems for which no metallicity dispersion measurement can be found in the literature. The solid line in the top left-hand panel corresponds to the luminosity–metallicity relation of Kirby et al. (2013) for dwarf spheroidals and dwarf irregulars. The dashed lines represent the RMS about this relation, also taken from Kirby et al. (2013). Among the 123 globular clusters presented here, the properties of 116 were extracted from Harris (1996) catalogue, revised in 2010. For the remaining ones (Kim 1, Kim 2, Kim 3, Laevens 1, Balbinot 1, Munoz 1, and SMASH 1), parameters of the discovery publications were used (Kim & Jerjen 2015, Kim et al. 2015, Kim et al. 2016, Laevens et al. 2014, Balbinot et al. 2013, Muñoz et al. 2012, and Martin et al. 2016c). Globular cluster metallicity spread measurements are taken from Willman & Strader (2012) and references therein: Carretta et al. (2006), Carretta et al. (2007), Carretta et al. (2009), Carretta et al. (2011), Cohen et al. (2010), Gratton et al. (2007), Johnson & Pilachowski (2010), and Marino et al. (2011). McConnachie (2012) and Willman & Strader (2012) are used to compile the properties of the dwarf galaxies represented here. The 18 dwarf galaxies represented here are Bootes I (Belokurov et al. 2006; Norris et al. 2010), Canes Venatici I (Zucker et al. 2006b), Canes Venatici II (Sakamoto & Hasegawa 2006), Coma Berinices, Hercules, Leo IV and Segue I (Belokurov et al. 2007), Draco and Ursa Minor (Wilson 1955), Fornax (Shapley 1938b), Leo I and Leo II (Harrington & Wilson 1950), Pisces II (Belokurov et al. 2010), Sculptor (Shapley 1938a), Sextans (Irwin et al. 1990), Ursa Major I (Willman et al. 2005b), Ursa Major II (Zucker et al. 2006a), and Willman I (Willman et al. 2005a). Their metallicity and metallicity spreads were drawn from Kirby et al. (2008), Kirby et al. (2010), Norris et al. (2010), and Willman et al. (2011). The dwarf galaxy candidates discovered recently and shown on this figure are Bootes II (Koch & Rich 2014), DES1 (Luque et al. 2016; Conn et al. 2018), Eridanus III (Bechtol et al. 2015; Koposov et al. 2015b; Conn et al. 2018), Hyades II (Martin et al. 2015), Pegasus III (Kim & Jerjen 2015), Reticulum II and Horologium I (Koposov et al. 2015a), Segue II (Belokurov et al. 2009), and the most significant candidates of Drlica-Wagner et al. (2015): Gru II, Tuc III, and Tuc IV.

or Boo II ($M_V \sim -2.7$) as shown in the bottom left-hand panel of Fig. 9. Regarding the size and Galactocentric distance of the satellite, Lae 3 can be compared to SMASH 1 (Martin et al. 2016c). SMASH 1 has a size of $9.1^{+5.9}_{-3.4}$ pc, and is lying at ~ 57 kpc of the centre of the Galaxy. The location and distance of SMASH 1 imply that it may be a satellite of the Large Magellanic Cloud. However, Lae 3 is brighter (-2.8 versus -1.0 mag) and is more metal-rich (-1.8 versus -2.2 dex). The top left-hand panel of Fig. 9 shows that the systemic metallicity of Lae 3 is offset by ~ 0.7 dex from the metallicity–luminosity relation of dwarf galaxies (Kirby et al. 2013). We have to turn to Pal 1 or Pal 13 (Harris 2010) to find a cluster with a luminosity comparable to the one of Lae 3 (respectively, of ~ -2.5 and ~ -3.8 mag). Still, these two GCs are much more compact, with a size of the order of the parsec.

Both the velocity and metallicity dispersions of Lae 3 are unresolved, although the small number of member stars in our spectroscopic data set does not give stringent enough constraints to rule out a dynamically hot system or that it is chemically enriched (right-hand panels of Fig. 9). Lae 3 is possibly mass segregated, which implies that its internal dynamics is ruled by purely baryonic two-bodies interactions (Kim et al. 2015) and it is statistically incompatible with the luminosity–metallicity relation of DGs. We therefore conclude that Lae 3 likely is an MW outer halo GC.

ACKNOWLEDGEMENTS

NL, NM, and RI gratefully acknowledge support from the French National Research Agency (ANR) funded project 'Pristine' (ANR-18-CE31-0017) along with funding from CNRS/INSU through the Programme National Galaxies et Cosmologie and through the CNRS grant PICS07708. ES, NM, and NL benefitted from the International Space Science Institute in Bern, CH because of the funding of the Teams 'The Formation and Evolution of the Galactic Halo' and 'Pristine'. This work has been published under the framework of the IdEx Unistra and benefits from a funding from the state managed by the French National Research Agency as part of the investments for the future program. This research was supported in part by the National Science Foundation under grant NSF PHY11-25915. DM is supported by an Australian Research Council (ARC) Future Fellowship (FT160100206). BPML gratefully acknowledges support from FONDECYT post-doctoral fellowship 3160510.

We gratefully thank the CFHT staff for performing the observations in queue mode, for their reactivity in adapting the schedule, and for answering our questions during the data-reduction process. We thank Nina Hernitschek for granting us access to the catalogue of Pan-STARRS variability catalogue.

Based on observations obtained at the CFHT, which is operated by the National Research Council of Canada, the Institut National des Sciences de l'Univers of the Centre National de la Recherche Scientifique of France, and the University of Hawaii.

Some of the data presented herein were obtained at the W. M. Keck Observatory, which is operated as a scientific partnership among the California Institute of Technology, the University of California, and the National Aeronautics and Space Administration. The Observatory was made possible by the generous financial support of the W. M. Keck Foundation. Furthermore, the authors wish to recognize and acknowledge the very significant cultural role and reverence that the summit of Maunakea has always had within the indigenous Hawaiian community. We are most fortunate to have the opportunity to conduct observations from this mountain.

The PS1 Surveys have been made possible through contributions of the Institute for Astronomy, the University of Hawaii, the Pan-STARRS Project Office, the Max-Planck Society and its participating institutes, the Max Planck Institute for Astronomy, Heidelberg and the Max Planck Institute for Extraterrestrial Physics, Garching, The Johns Hopkins University, Durham University, the University of Edinburgh, Queen's University Belfast, the Harvard-Smithsonian Center for Astrophysics, the Las Cumbres Observatory Global Telescope Network Incorporated, the National Central University of Taiwan, the Space Telescope Science Institute, the National Aeronautics and Space Administration under grant NNX08AR22G issued through the Planetary Science Division of the NASA Science Mission Directorate, the National Science Foundation under grant AST-1238877, the University of Maryland, and Eotvos Lorand University (ELTE).

This work has used data from the European Space Agency (ESA) mission *Gaia* (https://www.cosmos.esa.int/gaia), processed by the *Gaia* Data Processing and Analysis Consortium (DPAC, https://www.cosmos.esa.int/web/gaia/dpac/consortium). Funding for the DPAC has been provided by national institutions, in particular the institutions participating in the *Gaia* Multilateral Agreement.

REFERENCES

Arp H., van den Bergh S., 1960, PASP, 72, 48
Balbinot E. et al., 2013, ApJ, 767, 101
Baumgardt H., Makino J., 2003, MNRAS, 340, 227
Bechtol K. et al., 2015, ApJ, 807, 50
Bell E. F., de Jong R. S., 2001, ApJ, 550, 212
Belokurov V. et al., 2006, ApJ, 647, L111
Belokurov V. et al., 2007, ApJ, 654, 897
Belokurov V. et al., 2009, MNRAS, 397, 1748
Belokurov V. et al., 2010, ApJ, 712, L103
Belokurov V., Irwin M. J., Koposov S. E., Evans N. W., Gonzalez-Solares E., Metcalfe N., Shanks T., 2014, MNRAS, 441, 2124
Bland-Hawthorn J., Gerhard O., 2016, ARA&A, 54, 529
Boulade O. et al., 2003, SPIE, 4841, 72
Bovy J., 2015, ApJS, 216, 29
Carrera R., Pancino E., Gallart C., del Pino A., 2013, MNRAS, 434, 1681
Carretta E., Bragaglia A., Gratton R. G., Leone F., Recio-Blanco A., Lucatello S., 2006, A&A, 450, 523
Carretta E. et al., 2007, A&A, 464, 967
Carretta E. et al., 2009, A&A, 505, 117
Carretta E., Lucatello S., Gratton R. G., Bragaglia A., D'Orazi V., 2011, A&A, 533, A69
Chambers K. C. et al., 2016, preprint (arXiv:1612.05560)
Chantereau W., Charbonnel C., Meynet G., 2016, A&A, 592, A111
Cohen J. G., Kirby E. N., Simon J. D., Geha M., 2010, ApJ, 725, 288
Collins M. L. M. et al., 2010, MNRAS, 407, 2411
Conn B. C., Jerjen H., Kim D., Schirmer M., 2018, ApJ, 852, 68
Dotter A., Chaboyer B., Jevremović D., Kostov V., Baron E., Ferguson J. W., 2008, ApJS, 178, 89
Dotter A., Sarajedini A., Anderson J., 2011, ApJ, 738, 74
Drlica-Wagner A. et al., 2015, ApJ, 813, 109
Faber S. M. et al., 2003, SPIE, 4841, 1657
Gaia Collaboration, 2018, A&A, 616, A1
Gilmore G., Wilkinson M. I., Wyse R. F. G., Kleyna J. T., Koch A., Evans N. W., Grebel E. K., 2007, ApJ, 663, 948
Gratton R. G. et al., 2007, A&A, 464, 953
Harrington R. G., Wilson A. G., 1950, PASP, 62, 118
Harris W. E., 1996, AJ, 112, 1487
Harris W. E., 2010, preprint (arXiv:1012.3224)
Helmi A., Babusiaux C., Koppelman H. H., Massari D., Veljanoski J., Brown A. G. A., 2018, Nature, 563, 85
Ibata R., Sollima A., Nipoti C., Bellazzini M., Chapman S. C., Dalessandro E., 2011, ApJ, 738, 186
Irwin M., Lewis J., 2001, New Astron. Rev., 45, 105

Irwin M. J., Bunclark P. S., Bridgeland M. T., McMahon R. G., 1990, MNRAS, 244, 16P
Johnson C. I., Pilachowski C. A., 2010, ApJ, 722, 1373
Kim D., Jerjen H., 2015, ApJ, 799, 73
Kim D., Jerjen H., Milone A. P., Mackey D., Da Costa G. S., 2015, ApJ, 803, 63
Kim D., Jerjen H., Mackey D., Da Costa G. S., Milone A. P., 2016, ApJ, 820, 119
Kirby E. N., Simon J. D., Geha M., Guhathakurta P., Frebel A., 2008, ApJ, 685, L43
Kirby E. N. et al., 2010, ApJS, 191, 352
Kirby E. N., Cohen J. G., Guhathakurta P., Cheng L., Bullock J. S., Gallazzi A., 2013, ApJ, 779, 102
Koch A., Rich R. M., 2014, ApJ, 794, 89
Koposov S. et al., 2007, ApJ, 669, 337
Koposov S. E., Belokurov V., Torrealba G., Evans N. W., 2015a, ApJ, 805, 130
Koposov S. E. et al., 2015b, ApJ, 811, 62
Laevens B. P. M. et al., 2014, ApJ, 786, L3
Laevens B. P. M. et al., 2015, ApJ, 813, 44
Longeard N. et al., 2018, MNRAS, 480, 2609
Longeard N. et al., 2019, preprint (arXiv:1902.02780)
Luque E. et al., 2016, MNRAS, 458, 603
Mackey A. D. et al., 2010, ApJ, 717, L11
Madore B. F., Arp H. C., 1979, ApJ, 227, L103
Marino A. F. et al., 2011, A&A, 532, A8
Martin N. F. et al., 2015, ApJ, 804, L5
Martin N. F. et al., 2016a, MNRAS, 458, L59
Martin N. F. et al., 2016b, ApJ, 833, 167
Martin N. F. et al., 2016c, ApJ, 830, L10
McConnachie A. W., 2012, AJ, 144, 4
Muñoz R. R., Geha M., Côté P., Vargas L. C., Santana F. A., Stetson P., Simon J. D., Djorgovski S. G., 2012, ApJ, 753, L15
Norris J. E., Wyse R. F. G., Gilmore G., Yong D., Frebel A., Wilkinson M. I., Belokurov V., Zucker D. B., 2010, ApJ, 723, 1632
Pota V. et al., 2013, MNRAS, 428, 389
Renaud F., Agertz O., Gieles M., 2017, MNRAS, 465, 3622
Sakamoto T., Hasegawa T., 2006, ApJ, 653, L29
Schlafly E. F., Finkbeiner D. P., 2011, ApJ, 737, 103
Schlegel D. J., Finkbeiner D. P., Davis M., 1998, ApJ, 500, 525
Sesar B. et al., 2017, AJ, 153, 204
Shapley H., 1938a, Harvard College Observatory Bulletin, 908, 1
Shapley H., 1938b, Nature, 142, 715
Starkenburg E. et al., 2010, A&A, 513, A34
Strader J., Brodie J. P., Cenarro A. J., Beasley M. A., Forbes D. A., 2005, AJ, 130, 1315
The Dark Energy Survey Collaboration, 2005, preprint (astro-ph/0510346)
Willman B., Strader J., 2012, AJ, 144, 76
Willman B. et al., 2005a, AJ, 129, 2692
Willman B. et al., 2005b, ApJ, 626, L85
Willman B., Geha M., Strader J., Strigari L. E., Simon J. D., Kirby E., Ho N., Warres A., 2011, AJ, 142, 128
Wilson A. G., 1955, PASP, 67, 27
York D. G. et al., 2000, AJ, 120, 1579
Zucker D. B. et al., 2006a, ApJ, 650, L41
Zucker D. B. et al., 2006b, ApJ, 643, L103

This paper has been typeset from a TEX/LATEX file prepared by the author.